

X-RAY SOURCES AND THEIR OPTICAL COUNTERPARTS IN THE GLOBULAR CLUSTER M4

CEES BASSA¹, DAVID POOLEY², LEE HOMER³, FRANK VERBUNT¹, BRYAN M. GAENSLER⁴, WALTER H. G. LEWIN², SCOTT F. ANDERSON³, BRUCE MARGON⁵, VICTORIA M. KASPI^{6,2} AND MICHIEL VAN DER KLIS⁷

(Received February 6, 2004; Accepted March 19, 2004)

ABSTRACT

We report on the *Chandra X-ray Observatory* ACIS-S3 imaging observation of the Galactic globular cluster M4 (NGC 6121). We detect 12 X-ray sources inside the core and 19 more within the cluster half-mass radius. The limiting luminosity of this observation is $L_x \approx 10^{29}$ erg s⁻¹ for sources associated with the cluster, the deepest X-ray observation of a globular cluster to date. We identify 6 X-ray sources with known objects and use *ROSAT* observations to show that the brightest X-ray source is variable. Archival data from the *Hubble Space Telescope* allow us to identify optical counterparts to 16 X-ray sources. Based on the X-ray and optical properties of the identifications and the information from the literature, we classify two (possibly three) sources as cataclysmic variables, one X-ray source as a millisecond pulsar and 12 sources as chromospherically active binaries. Comparison of M4 with 47 Tuc and NGC 6397 suggests a scaling of the number of active binaries in these clusters with the cluster (core) mass.

Subject headings: binaries: close — globular clusters: general — globular clusters: individual (M4, NGC 6121) — novae, cataclysmic variables, contact binaries — X-rays: stars

1. INTRODUCTION

Faint X-ray sources ($L_x \lesssim 10^{35}$ erg s⁻¹) were first discovered in observations made with the *Einstein* and *ROSAT* observatories (Hertz & Grindlay 1983; Verbunt 2001). It was only with *Chandra*, however, that a large number of faint sources was identified: more than one hundred in 47 Tuc, and up to a few dozen each in e.g. NGC 6397, NGC 6752, NGC 6440, and ω Cen (Grindlay et al. 2001a,b; Pooley et al. 2002a,b; Rutledge et al. 2002). These faint sources represent a mix of objects with different X-ray luminosities. Brightest are the neutron stars accreting at a low rate from a companion (quiescent low mass X-ray binaries or qLMXBs), followed by white dwarfs accreting from low-mass companions (cataclysmic variables or CVs). The active binaries (ABs) tend to be the faintest, while radio pulsars with short periods (millisecond or recycled pulsars, MSPs) have X-ray luminosities in a similar range as CVs. The three types of chromospherically or magnetically active binaries are detached binaries of two main sequence stars (BY Dra systems), detached binaries of a main sequence star and a giant or a sub-giant (RS CVn systems) and contact

binaries (W UMa systems).

Globular clusters contain many more neutron star binaries per unit mass than the galactic disk. Hence, in a globular cluster one finds a binary with a neutron star (which is rather difficult to make via ordinary evolution of an initial binary), it is highly probable that this binary was formed via a close encounter between stars (Fabian et al. 1975; Hills 1976). Isolated millisecond pulsars in globular clusters are thought to have been formed in such binaries, and thus are probably also a result of close stellar encounters.

On the other hand, binaries that are common in the field, are more likely to be of primordial origin in globular cluster, including the chromospherically active binaries. Cataclysmic variables are relatively common in the Galactic disk, and those in globular clusters could in principle originate from primordial binaries or stellar encounters. Pooley et al. (2003) showed that the number of faint sources above the threshold $L_x > 4 \times 10^{30}$ erg s⁻¹ in a cluster scales with its collision number Γ , which is a theoretical estimate for the number of close encounters. Since the majority of such sources are cataclysmic variables, this suggests that most cataclysmic variables in globular clusters are in fact formed via close stellar encounters.

Most clusters investigated with *Chandra* so far have relatively high collision numbers (see e.g. Table 1 in Pooley et al. 2003); because the limit to which X-ray sources in these clusters could be detected is relatively high, most X-ray sources known in these clusters are either neutron stars (accreting or radio pulsars), or cataclysmic variables. So far, a sizable number of X-ray sources has been identified as chromospherically active binaries only in 47 Tuc (Edmonds et al. 2003a,b). In this paper, we discuss a globular cluster with a relatively low collision number, M4 (NGC 6121). This cluster is a relatively nearby cluster with a moderate absorption ($d = 1.73$ kpc, $A_V = 1.32$, Richer et al. 1997). The core and half-mass radii of M4 are 49''8 and 3'65, respectively (Harris 1996).

¹ Astronomical Institute, Utrecht University, PO Box 80 000, 3508 TA, Utrecht, The Netherlands; c.g.bassa@astro.uu.nl, f.w.m.verbunt@astro.uu.nl.

² Center for Space Research and Department of Physics, Massachusetts Institute of Technology, 70 Vassar Street, Building 37, Cambridge, MA 02139-4307; davep@space.mit.edu, lewin@space.mit.edu.

³ Department of Astronomy, University of Washington, Box 351580, Seattle, WA 98195-1580; homer@astro.washington.edu, anderson@washington.edu.

⁴ Harvard-Smithsonian Center for Astrophysics, 60 Garden Street, Cambridge, MA 02138; bgaensler@cfa.harvard.edu.

⁵ Space Telescope Science Institute, 3700 San Martin Drive, Baltimore, MD 21218; margon@stsci.edu

⁶ Department of Physics, McGill University, Ernest Rutherford Physics Building, 3600 University Street, Montreal, QC H3A 2T8, Canada; vkaspi@hep.physics.mcgill.ca

⁷ Astronomical Institute “Anton Pannekoek”, University of Amsterdam, Kruislaan 403, 1098 SJ, The Netherlands; michiel@science.uva.nl

We use these values throughout the paper.

A priori, we would thus expect that the majority of X-ray sources in this cluster to be chromospherically active binaries. That chromospherically active binaries exist in this cluster is evident from optical studies. For example, Kaluzny et al. (1997) discovered a number of optical variables, including several contact binaries.

The presence of a recycled radio pulsar PSR B1620–26 (Lyne et al. 1988) in M4 is remarkable, but can be explained by noting that the small collision numbers of many globular clusters still add up, so that at least some of the clusters with small Γ should contain a binary with a neutron star (Verbunt & Hut 1987). PSR B1620–26 is in a 191 day orbit around a white dwarf of $\sim 0.3 M_{\odot}$; the binary is accompanied by a third object of planetary mass in an orbit of ~ 100 years (Thorsett et al. 1999; Sigurdsson et al. 2003).

2. X-RAY OBSERVATIONS AND ANALYSIS

M4 was observed for 25.8 ks on 2000 June 30 with the Advanced CCD Imaging Spectrometer (ACIS) on the *Chandra X-ray Observatory* with the telescope aimpoint on the back-side illuminated S3 chip. The data were taken in timed-exposure mode with the standard integration time of 3.24 s per frame and telemetered to the ground in faint mode.

Data reduction was performed using the CIAO 2.3 software provided by the *Chandra X-ray Center* (CXC)⁸. We reprocessed the data using the CALDB 2.21 set of calibration files (gain maps, quantum efficiency, quantum efficiency uniformity, effective area) without including the pixel randomization that is added during standard processing. This method slightly improves the point spread function. We filtered the data using the standard *ASCA* grades, and we excluded both bad pixels and software-flagged cosmic ray events. Intervals of background flaring were searched for, but none were found, hence we simply applied the good-time intervals supplied by the CXC.

2.1. Source Detection

The CIAO wavelet-based *wavdetect* tool was employed for source detection in both the 0.5–6.0 keV band and 0.3–10.0 keV band. We detected 41 sources on the entire S3 chip in the 0.5–6.0 keV band; for the *wavdetect* settings we used, approximately one of those detections may be spurious. Of these sources, 30 lie within the half-mass radius of the cluster.

We also searched part of the adjacent S4 CCD since part of the half-mass region fell on this chip, but no sources were detected in this area. One additional source was detected on S3 in the broader 0.3–10.0 keV band with three counts, two of which were between 8 and 10 keV. The significance of this source, as well as its possible membership of the cluster, is questionable. For completeness, however, we leave it in our source list (Table 1) as the last source. The sources are numbered according to detected counts in the 0.5–6.0 keV band.

From the $\log N - \log S$ relationships of Giacconi et al. (2001), we expect between 5 and 6 background sources within the cluster half-mass radius. However, as M4 is located towards the bulge of the galaxy ($l = 351.0^{\circ}$, $b = 16.0^{\circ}$, Harris 1996) this relation would underestimate

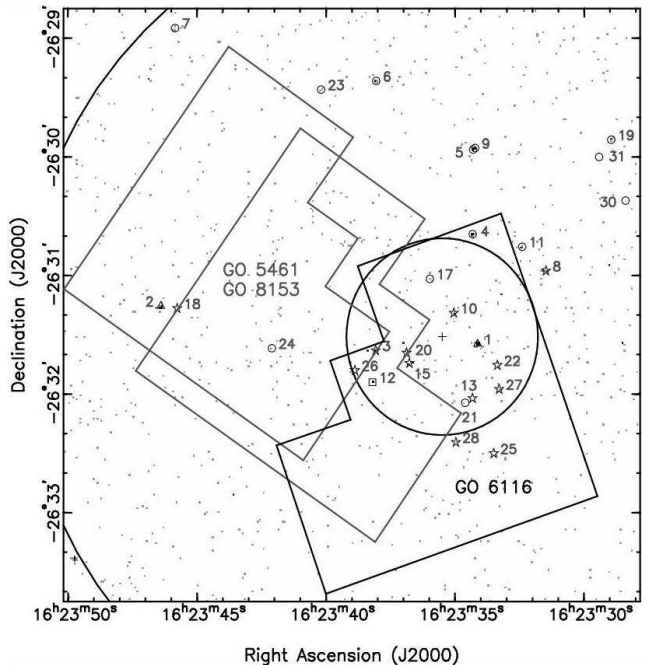


FIG. 1.— X-ray image of a $5' \times 5'$ region of M4. Shown are all counts in the 0.5–6.0 keV range. The cluster center, core and half-mass radii are indicated by a cross and two circles, respectively (Harris 1996). The detected X-ray sources are marked and numbered, omitting the “CX” prefix. X-ray sources classified as cataclysmic variables are indicated with triangles, chromospherically active binaries with stars, millisecond pulsars with squares and unclassified or ambiguous sources are indicated with circles. See Section 4 for the source classification. Also shown are three archival pointings of the *HST*/WFPC2 used to locate optical counterparts to the *Chandra* X-ray sources.

the galactic contribution of background sources and provide a lower limit only. We have analyzed ACIS-S3 data from the October 15, 2002 *Chandra* observation of the low-mass X-ray binary (LMXB) MXB 1659–298, which has $l = 353.8^{\circ}$ and $b = 7.3^{\circ}$. In the 27 ks of this observation the 1/4 sub-array of the S3 CCD shows 5 sources, other than the LMXB itself, in the 0.5–6.0 keV band. Scaling this up to the whole chip and taking into account Poissonian errors would give rise to some 20 sources within an area of the size of the M4 half-mass radius. Given that MXB 1659–298 is located about 10° closer to the galactic center this would overestimate the number of background sources towards M4. Though both limit determinations are very different in nature, we expect 6 to 20 background sources within the half-mass radius of M4, and zero or one within the core.

All sources are consistent with being point sources. However, CX5 and CX9 overlap somewhat. They were identified by *wavdetect* as two separate sources. It is possible that they are actually a single extended object, but the double-peaked nature of the image lends support to the interpretation as two point sources.

There is some evidence for excess emission on the approximately 32200 pixels inside the core radius. The residual number of counts (i.e., the total counts minus those due to the 12 point sources inside the core) in the 0.5–6.0 keV band is 438 ± 20 counts, while we would expect 287 ± 15 background counts on the basis of the number of counts that we measure in a source-free region

⁸ <http://asc.harvard.edu>

outside the core. This excess emission could be due to either unresolved point sources or diffuse emission.

A $5' \times 5'$ portion of the *Chandra* exposure of M4 is shown in Figure 1. The detected sources are encircled and numbered. The cross indicates the cluster center, while the circles denote the core and half-mass radius.

2.2. Count Rates

We extracted source counts in the following bands: 0.5–1.5 keV (X_{soft}), 0.5–4.5 keV (X_{med}), and 1.5–6.0 keV (X_{hard}). The detected count rate was corrected for background, exposure variations, and foreground photoelectric absorption. We make these corrections in order to produce an X-ray color-magnitude diagram (CMD) that can be compared to the X-ray CMDs that have resulted from *Chandra* observations of other globular clusters. In addition, however, attention must be paid to differences in detector responses and, of course, exposure times and distances.

The background count rate in each band was estimated from a source-free region on the S3 chip outside the core and to the northwest. The density of background counts in each band (for the 25.8 ksec observation) is 0.0043 counts pixel $^{-1}$ in X_{soft} , 0.0077 counts pixel $^{-1}$ in X_{med} , and 0.0047 counts pixel $^{-1}$ in X_{hard} . The background count rate in the core may be somewhat higher, but even factors of a few greater than this estimate have negligible effects on our analysis.

In general, the exposure variations among sources were at the $\sim 7\%$ level or less, but CX30 had an exposure which was 20% less than the others. To account for these variations in exposure, we applied multiplicative corrections based on the ratio of the average effective area of the detector at the location of a source in each of the three bands to that in the same band of CX6, which had the highest average exposure. The individual effective area curves for the sources were made using the CIAO tool *mkarf*. The average effective area of the detector at the location of CX6 in each of the bands was 538 cm 2 (X_{soft}), 451 cm 2 (X_{med}), and 376 cm 2 (X_{hard}).

While the previous corrections were relatively minor (at the few percent level or less), the correction for photoelectric absorption is appreciable for M4. The conversion of optical extinction to column density (Predehl & Schmitt 1995) gives a value of $N_H = 2.36 \times 10^{21}$ cm $^{-2}$. We investigated the effects of such an absorption on three characteristic spectra: a 3 keV thermal bremsstrahlung, a 0.3 keV blackbody plus power law with photon index of $\Gamma = 2$, and a power law with a photon index of $\Gamma = 2$. The effects were most prominent in the X_{soft} band, where the absorbed count rate was a factor of 2.2–2.5 lower than the unabsorbed one (depending on the spectrum). Averaging the results of each spectrum in each band, we use the following correction factors: 2.38 (X_{soft}), 1.87 (X_{med}), and 1.10 (X_{hard}). Table 1 lists both the observed and fully corrected counts in each band. The effect of the absorption correction on the X-ray CMD (Fig. 2) is a uniform shift of all points 0.27 units on the left axis and 0.34 units on the bottom axis. The bottom and left axes give the X-ray color and magnitude without this shift (they do, however, include the small corrections for background subtraction and exposure variations).

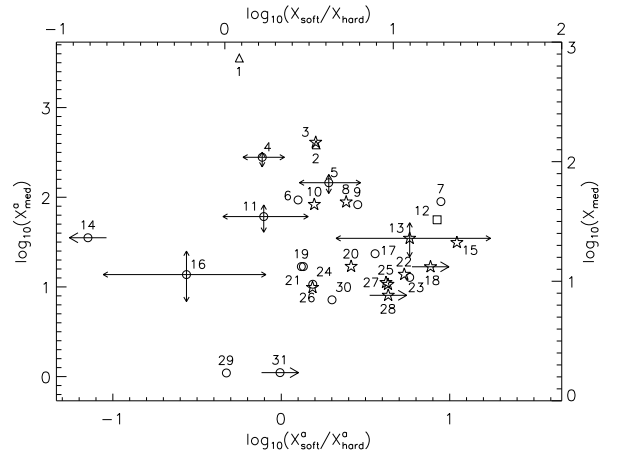


FIG. 2.— X-ray color-magnitude diagram. The X-ray color is defined as the logarithm of the ratio of X_{soft} (0.5–1.5 keV) corrected counts to X_{hard} (1.5–6.0 keV) corrected counts, and the magnitude is the logarithm of X_{med} (0.5–4.5 keV) corrected counts. Our correction for photoelectric absorption has the effect of uniformly shifting the data +0.27 units on the left axis and +0.34 units on the bottom axis. The bottom and left axes provide the absorbed color and magnitude scales (a), i.e., the observed colors and magnitudes uncorrected for absorption. For the sake of clarity, only a few error bars (1σ) are shown. Sources CX14, CX18, CX28 and CX31 were not detected in either the X_{soft} or X_{hard} band, respectively. We illustrate their limits on $\log X_{\text{soft}}/X_{\text{hard}}$ by adopting a single count in these bands. The X-ray sources are marked as in Fig. 1. See Section 4 for the source classification.

2.3. Spectral Fitting

We used the CIAO tool *dmextract* to extract spectra of sources CX1–CX4 in the 0.3–10 keV range. We binned the spectra to have at least 10 counts (20 counts for CX1) per bin and fit them in XSPEC (Arnaud 1996) using χ^2 statistics.

For CX2, CX3, and CX4, three different models (with absorption) were fit: thermal bremsstrahlung (TB), blackbody with a small ($\sim 20\%$) power-law contribution (BB+PL), and power law (PL). We fixed N_H to the value from optical extinction. As expected for such low-count spectra, very few fits could be formally ruled out. We estimated the unabsorbed source luminosities by averaging the results from the three best-fit models for each source. The spread in L_x of the three models was $\sim 15\%$ for each source. Fitting a linear relation to these luminosities versus corrected X_{med} counts, we have estimated the unabsorbed luminosities for sources CX5–CX31 based on their X_{med} counts (note though that any differences between spectra are not accounted for). These are listed in Table 1.

The X-ray color and magnitude of CX1 (Fig. 2) suggested that it might be a CV, but the spectral fits using an absorbed TB model (with N_H allowed to vary) preferred the maximum temperature allowed by the model in XSPEC, namely, $kT = 200$ keV, which gave a $\chi^2/\text{d.o.f.}$ of 36.0/39. Fixing the temperature at the more reasonable value of $kT = 25$ keV still allowed for a statistically acceptable fit ($\chi^2/\text{d.o.f.}$ of 42.1/40). The TB results indicated a rather hard spectrum, and an absorbed PL model (again with N_H allowed to vary) gave a best-fit photon index of 0.99 ± 0.17 and best-fit N_H of $(2.6^{+1.1}_{-0.7}) \times 10^{21}$ cm $^{-2}$ with a $\chi^2/\text{d.o.f.}$ of 33.3/39. The PL fit is shown in Fig. 3, and the unabsorbed luminosity

TABLE 1. M4 X-RAY SOURCES

Source ^a	R.A. (J2000.0) ^b	Decl. (J2000.0) ^b	Detected Counts/Corrected Counts ^c			$L_x(0.5\text{--}2.5\text{ keV})$ (ergs s ⁻¹) ^d	Counterpart ^e	ID ^f
			X _{soft}	X _{med}	X _{hard}			
CX 1...	16 23 34.128 (1)	-26 31 34.85 (2)	154/381.2	379/736.4	275/313.0	8.3×10^{31}	Opt.?./R9?	CV
CX 2...	16 23 46.399 (3)	-26 31 15.67 (8)	48/117.5	72/138.3	30/33.8	6.0×10^{30}	Opt.	CV
CX 3...	16 23 38.073 (3)	-26 31 38.18 (4)	46/113.6	75/145.2	29/32.8	5.4×10^{30}	Opt.	AB
CX 4...	16 23 34.321 (4)	-26 30 39.27 (5)	28/68.8	56/108.9	36/41.3	3.6×10^{30}	Opt.	CV/AB
CX 5...	16 23 34.300 (4)	-26 29 56.47 (6)	23/55.6	35/66.7	12/13.4	2.5×10^{30}	V56	amb.
CX 6...	16 23 38.058 (9)	-26 29 21.81 (14)	15/35.2	26/47.8	12/12.9	1.8×10^{30}	–	
CX 7...	16 23 45.848 (12)	-26 28 55.03 (19)	23/54.9	25/46.3	3/2.9	1.8×10^{30}	Opt.	fg.
CX 8...	16 23 31.478 (9)	-26 30 57.84 (7)	17/41.2	24/46.0	7/7.8	1.7×10^{30}	V52	AB
CX 9...	16 23 34.224 (5)	-26 29 55.69 (5)	17/41.0	23/43.7	6/6.7	1.7×10^{30}	V56	amb.
CX 10...	16 23 35.047 (8)	-26 31 19.18 (7)	14/34.0	23/43.9	9/10.0	1.7×10^{30}	Opt.	AB
CX 11...	16 23 32.399 (7)	-26 30 45.63 (6)	8/19.4	18/34.7	10/11.4	1.3×10^{30}	–	
CX 12...	16 23 38.205 (4)	-26 31 54.21 (6)	16/39.3	17/32.7	2/2.2	1.2×10^{30}	Rad./Opt.	MSP
CX 13...	16 23 34.326 (7)	-26 32 02.33 (10)	11/26.9	12/22.9	2/2.1	8.7×10^{29}	Opt./V49	AB
CX 14...	16 23 25.948 (15)	-26 33 54.62 (10)	0/–	12/23.1	12/13.9	8.7×10^{29}	–	
CX 15...	16 23 36.769 (8)	-26 31 44.60 (11)	10/24.6	11/21.1	1/1.0	8.0×10^{29}	Opt./V48	AB
CX 16...	16 23 33.682 (6)	-26 34 17.27 (10)	2/4.7	6/11.4	7/7.9	4.3×10^{29}	–	
CX 17...	16 23 35.975 (11)	-26 31 01.89 (8)	7/16.9	9/17.0	2/2.2	6.4×10^{29}	–	
CX 18...	16 23 45.767 (9)	-26 31 16.85 (14)	7/17.0	7/13.2	0/–	5.0×10^{29}	Opt./V55	AB
CX 19...	16 23 28.953 (8)	-26 29 51.47 (9)	4/9.5	7/13.3	3/3.3	5.0×10^{29}	–	
CX 20...	16 23 36.881 (11)	-26 31 39.43 (15)	5/12.2	7/13.3	2/2.2	5.0×10^{29}	Opt.	AB
CX 21...	16 23 34.610 (5)	-26 32 04.60 (19)	4/9.7	7/13.3	3/3.3	5.0×10^{29}	Opt.	
CX 22...	16 23 33.362 (9)	-26 31 45.65 (15)	5/12.2	6/11.4	1/1.1	4.3×10^{29}	Opt.	AB
CX 23...	16 23 40.189 (20)	-26 29 26.10 (25)	5/11.6	6/10.8	1/0.9	4.1×10^{29}	–	
CX 24...	16 23 42.096 (12)	-26 31 37.03 (13)	3/7.2	5/9.4	2/2.2	3.6×10^{29}	Opt.	amb.
CX 25...	16 23 33.503 (9)	-26 32 30.28 (8)	4/10.0	5/9.8	1/1.1	3.7×10^{29}	Opt.	AB
CX 26...	16 23 38.884 (11)	-26 31 48.26 (8)	3/7.3	5/9.5	2/2.2	3.6×10^{29}	Opt.	AB
CX 27...	16 23 33.290 (5)	-26 31 57.81 (25)	4/9.7	5/9.4	1/1.0	3.6×10^{29}	Opt.	AB
CX 28...	16 23 34.969 (12)	-26 32 24.65 (10)	4/9.9	4/7.6	0/–	2.9×10^{29}	Opt.	AB
CX 29...	16 23 19.486 (19)	-26 31 43.39 (26)	1/2.3	1/1.7	2/2.3	6.5×10^{28}	–	
CX 30...	16 23 28.396 (9)	-26 30 22.25 (23)	2/5.9	3/7.0	1/1.4	2.6×10^{29}	–	
CX 31...	16 23 29.424 (9)	-26 30 00.19 (11)	1/2.3	1/1.7	0/–	6.5×10^{28}	–	

^aSources are numbered according to their total counts.

^bThe *Chandra* positions have been corrected for a shift of $0''.15$ in declination (see §3.2). Positional uncertainties are given in parentheses and refer to the last quoted digit and are the centroiding uncertainties given by *wavdetect*.

^cCorrections are described in Sect. 2.2. The X-ray bands are 0.5–1.5 keV (X_{soft}), 0.5–4.5 keV (X_{med}) and 1.5–6.0 keV (X_{hard}).

^dFor sources CX1–CX4, L_x comes from an average of the best-fit models for each source (Sect. 2.3). A linear relation between L_x and X_{med} counts for these sources was derived and used to estimate L_x for sources CX5–CX31 based on their X_{med} counts. Typical uncertainties in L_x are $\sim 15\%$.

^eType of counterpart (optical and/or radio) found and associations (if any) with previously reported sources. The “V” numbers refer to optical variables by Kaluzny et al. (1997) and Mochejska et al. (2002). R9 is an X-ray source detected by *ROSAT* (Verbunt 2001).

^fClassification of the sources; see Sect. 4. The abbreviation MSP stands for millisecond pulsar, CV for cataclysmic variable and AB for active binary. Sources for which the classification is ambiguous are abbreviated with *amb.* and the foreground source CX7 is classified as *fg.*. See text for details.

from this model is 6.8×10^{31} erg s⁻¹ in the 0.5–2.5 keV band.

3. OPTICAL OBSERVATIONS

Three fields located inside the half-mass radius have been observed with the Wide Field Planetary Camera 2 (WFPC2) aboard the *Hubble Space Telescope* (*HST*), and are shown in Fig. 1. Deep observations (dataset GO-5461) of three fields were obtained to determine the mass and luminosity functions of the main and white dwarf sequence (Richer et al. 1995, 1997) and two of these fields (see Fig. 1, gray outlines) fall within the cluster half-mass radius. These two fields were imaged for 11 800 s in F336W (hereafter U_{336}), 15 000 s in F555W (V_{555}) and 5 500 s in F814W (I_{814}) and were re-observed in I_{814} , with exposure times of 5 680 s, (GO-8153) approximately 5 years later. This allowed separation of field stars from the low luminosity cluster members through proper motion properties (Bedin et al. 2001). Finally there exist

shallow (249 s) V_{555} and (249 s) I_{814} observations (GO-6116) originally obtained to search for the optical counterpart of PSR B1620–26. These observations (Fig. 1, black outline) cover nearly the entire region enclosed by the core radius. Of the 31 sources listed in Table 1, 18 coincide with the three *HST*/WFPC2 fields.

This section outlines the data reduction, photometry and astrometry of the *HST*/WFPC2 images.

3.1. Data Reduction and photometry

The single *HST* images and the association products⁹ were obtained from the ESO archive. The single images were already calibrated, including full bias subtraction and flat-fielding. The association products consist of co-added, cosmic-ray cleaned images and association files, which contain the shifts between the single images. These shifts were used as input for the further reduction

⁹ http://archive.eso.org/archive/hst/wfpc2_asn/

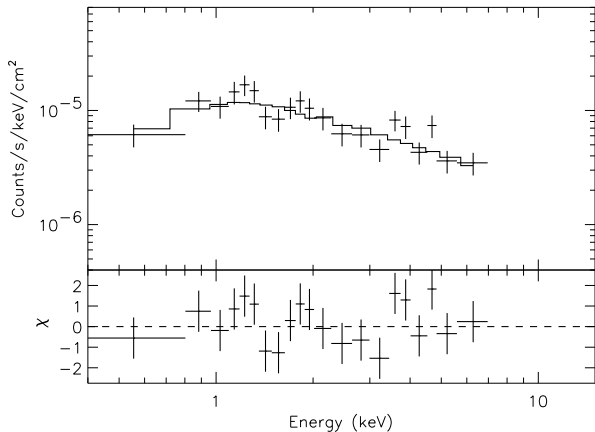


FIG. 3.— *Chandra* spectrum of the brightest source, CX1. Datapoints are shown as crosses in the top panel, and an absorbed power-law model is shown as a solid line; residuals from this fit are shown in the bottom panel. Both the data and model have been divided by the instrument effective area for the purpose of plotting.

of the data, using HSTphot 1.1 (Dolphin 2000a). This package is especially written for the reduction and photometry of *HST* images.

First, the HSTphot task *mask* was used on each image to mask bad pixels and image defects. This ensures that these pixels are not used in the further analysis. The task *crmask* was used to remove the cosmic ray hits, which are widely present in the separate images. For each filter the images were compared against each other to remove the cosmic ray events. The HSTphot task *hotpixels* was then used to mask the known hot pixels in the WFPC2 detectors.

To obtain photometry for each individual image we used the photometry task *hstphot* of HSTphot 1.1. This task takes as input all available images in each filter and produces a master list of positions and magnitudes for each star found. The positions and magnitudes are determined by fitting a model point spread function (PSF), to each star. After all stars are fitted it calculates aperture corrections and corrects for the charge transfer efficiency effect. These corrections, together with the zero-points are described in (Dolphin 2000b).

3.2. Astrometry

To search for optical counterparts to the *Chandra* X-ray sources we aim to place both the X-ray and the optical frame onto the International Celestial Reference System (ICRS). We use this approach to improve the absolute pointing accuracy of *Chandra* and *HST*, $0''.6$ and $1''.0$ (1σ) respectively (Aldcroft et al. 2000; Biretta et al. 2000).

To place the *HST* images onto the ICRS we use two intermediate steps; first, we align a ground-based image onto the ICRS using an astrometric catalog, then we align the *HST* images onto the ground-based image. To bring the X-ray frame onto the ICRS we use three optical identifications of X-ray sources.

3.2.1. Astrometry of the *HST* images

A 2 minute *V*-band image, taken on February 21, 2002 with the Wide Field Imager (WFI) at the ESO 2.2 me-

ter telescope on La Silla, was retrieved from the ESO archive and used to calibrate the *HST*/WFPC2 images. The WFI has an array of 8 CCDs, each CCD having a $8' \times 16'$ field of view, giving a total of $33' \times 34'$. M4 is roughly centered on one chip, and, to minimize the effects of geometric distortion, an $8' \times 8'$ sub-image, containing the entire area within the half-mass radius, was extracted from this chip.

We found 115 stars on this sub-image that matched entries in the USNO CCD Astrograph Catalog (UCAC1, Zacharias et al. 2000). Of these stars, 91 were not saturated and appeared stellar and unblended and were used to compute an astrometric solution, fitting for zero-point position, scale and position angle. Five outliers, having residuals larger than $0''.2$ were rejected from the fit. The final solution has rms residuals of $0''.05$ in both coordinates.

We calibrate the *HST* frames with the astrometric solution of the WFI image. First, the pixel positions of the stars in the *HST* datasets are placed on a single metaframe using the geometric distortion corrections and relative chip positions/orientations found by Anderson & King (2003). Next, using the astrometric solution in the FITS header of the *HST* images, nominal celestial coordinates are computed for some 300–400 of the brightest stars. These positions are then matched with stars on the WFI image and their centroids are measured. Similar selection criteria for saturation and blending are used as with the UCAC stars. An astrometric solution is calculated from the calibrated celestial coordinates and the metaframe positions of the *HST* stars. Outliers having residuals larger than three times the rms residual of the fit are removed, and a new solution is computed. This process is iterated until convergence. On average after convergence the astrometric solution contained some 200 stars with rms residuals of $0''.07$ in both right ascension and declination.

The 1σ uncertainty in the optical positions is $0''.12$, the quadratic sum of the positional uncertainty in the tie of the WFI image to the UCAC ($0''.07$) and the uncertainty in the transfer to the *HST* frames ($0''.09$) and the uncertainty in the tie of the UCAC onto the ICRS ($0''.02$, Assafin et al. 2003).

By placing the *HST* and WFI observations onto the ICRS with the UCAC we effectively set these images at the epoch of the UCAC observation, which is 1999.4. This implies that any average proper motion between the epochs of the *HST* and WFI observations has been removed.

The difference in proper motion between cluster members and background stars (Bedin et al. 2003) possibly explains why our uncertainty in the calibration between *HST* and WFI is larger than what we have found for similar calibrations of data from other clusters (e.g. Bassa et al. 2003).

3.2.2. Astrometry of the *Chandra* frame

We use three optical identifications in the *HST* data of the *Chandra* X-ray sources to place the X-ray frame onto the ICRS frame of the *HST*/WFPC2 images: the white dwarf companion of PSR B1620–26 and two W UMA variables.

At the UCAC epoch, 1999.4, the position of PSR B1620–26 is $\alpha_{J2000} = 16^{\text{h}}23^{\text{m}}38^{\text{s}}.2147(5)$, $\delta_{J2000} =$

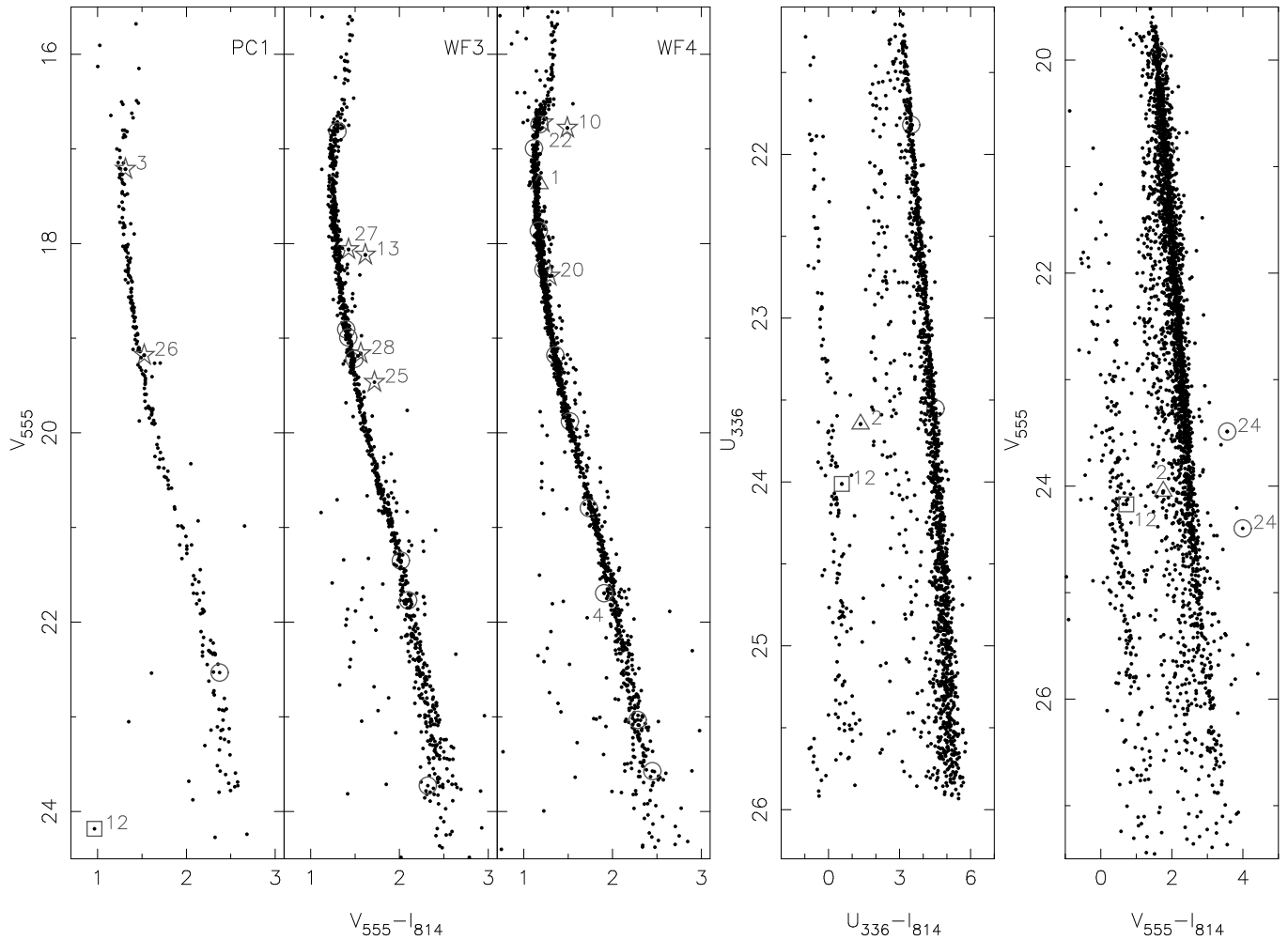


FIG. 4.— Color-magnitude diagrams (CMDs) of the *HST*/WFPC2 observations of M4. The first three panels show CMDs from the GO-6116 dataset for the PC1, WF3 and WF4 chips, respectively (no X-ray sources coincide with the WF2 chip). The fourth and fifth panel show two CMDs of the data in both GO-5461 fields. All stars inside the 95% confidence error circles are marked, while the candidate counterparts are numbered. The X-ray sources are marked as in Fig. 1. The candidate counterpart to CX24 is plotted twice, as it was observed in both fields of the GO-5461 dataset and had varied in brightness. The candidate counterpart was brightest during the observation of the field closest to the core of M4.

$-26^{\circ}31'53''.95(4)$, where we use the position and proper motion from Thorsett et al. (1999). According to our optical astrometry, this position is compatible with a white dwarf, at an offset of $-0''.04 \pm 0''.09$ ($-0''.003 \pm 0''.006$) in right ascension and $0''.07 \pm 0''.10$ in declination for the GO-5461 dataset. (The uncertainty in this offset is the quadratic sum of the uncertainty in the optical astrometry and the uncertainty in the corrected pulsar position.) With our accurate position ($0''.12$) for the white dwarf, we confirm the identification by Sigurdsson et al. (2003) and Richer et al. (2003) of this white dwarf as the companion of the pulsar. The position of X-ray source CX12 coincides with that of PSR B1620–26.

Five optical variables found by Kaluzny et al. (1997) and Mochejska et al. (2002), roughly coincide with *Chandra* X-ray sources, three of which are in the *HST* field(s) of view. Comparison of the Kaluzny et al. (1997) finding charts with our WFI and *HST* images shows that the variables are indeed excellent matches to the X-ray sources. The three variables coincident with the *HST* images are all identified as W UMa binaries. V55/CX18 is a single star on the *HST* images, and we are confident that

it is the star responsible for the optical variability. However, the variables V48 and V49 both are blends of four and two stars respectively. In the case of CX13/V49 one of the stars is clearly above the main sequence, indicating that this star is the variable. However, for CX15/V48 all stars of the blend lie on the main-sequence, and none of these can be securely identified as the variable.

We therefore use the optical positions of the white dwarf companion to PSR B1620–26 and the variables V49 and V55 to compute the shift needed to place the X-ray positions of CX12, CX13 and CX18 onto the optical positions. We have a total of 6 measurements, as CX12 is in the field of view of datasets GO-6116, GO-5461 and GO-8153, CX13 only in that of GO-6116 and CX18 in those of GO-5461 and GO-8153. The weighted average shift is $0''.00 \pm 0''.05$ in right ascension and $0''.15 \pm 0''.05$ in declination, well within the 1σ uncertainty of the absolute *Chandra* pointing accuracy. We apply this shift as a boresight correction to the X-ray positions.

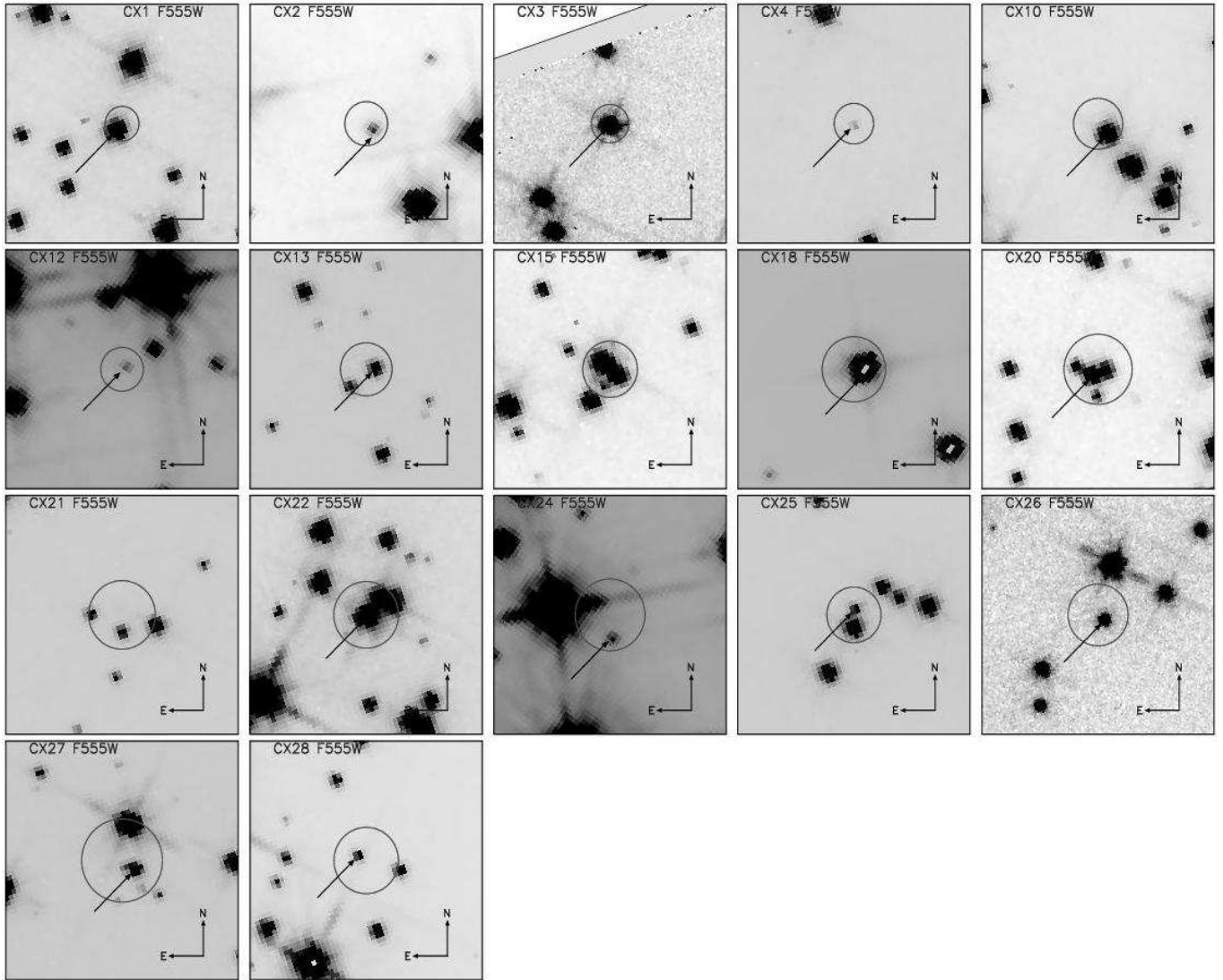


FIG. 5.— $5'' \times 5''$ finding charts for the candidate optical counterparts. The finding charts are constructed from the coadded V_{555} “association” images. For sources CX2, CX12, CX18 and CX24, images from the GO-5461 dataset were used, images from the GO-6116 dataset are used for the other candidate counterparts. The 95% confidence uncertainties on the *Chandra* positions are overlaid on these charts, while the candidate counterparts are indicated with an arrow. No arrow is present for sources CX15 and CX21 as no candidate counterparts were found. The pixel scale varies between sources coincident with WF chips and the PC1 chip (CX3 and CX26). The greyscale of these images is chosen as such to enhance the visibility of the candidate counterparts.

3.3. Identification of counterparts in the HST images

We search for optical/UV stars inside 95% confidence radii of the *Chandra* sources positions. The 1σ uncertainty in a source position is the quadratic sum of the positional uncertainty for the X-ray source (Table 1), the uncertainty in the optical astrometry ($0''.12$) and the uncertainty in the X-ray boresight correction ($0''.07$). The 95% confidence radius is a factor $[-2 \log(1 - 0.95)]^{1/2} = 2.448$ larger than the 1σ uncertainty in the position.

Each of the X-ray source error circles was visually checked for stars that were not found during the initial run of *hstphot*. Stars that were missed were added by hand and the photometry task was executed again.

The resulting photometry lists were used to create a set of color-magnitude diagrams (CMDs), shown in Figure 4. The data from the GO-6116 dataset is separated into three panels, one for each *HST*/WFPC2 chip con-

taining X-ray sources, as the cluster main sequence is displaced by about 0.1 magnitude in $V_{555} - I_{814}$ between the individual chips. Differential reddening towards M4 (Cudworth & Rees 1990) is the likely cause for this. The data from the two GO-5461 fields, shown in the last two panels, did not display these displacements in color and the data from all four chips is plotted.

We used the *hstphot* information indicating the goodness of fit for a star to exclude the diffraction spike artifacts from the star list. These artifacts are widely present, especially in the GO-5461 dataset, which had the longest exposures. For more information we refer to the *HSTphot* 1.1 manual¹⁰.

All stars within the 95% confidence radii of the *Chandra* source positions are marked in Figure 4. Stars with colors abnormal with respect to the cluster main se-

¹⁰ <http://www.noao.edu/staff/dolphin/hstphot/>

TABLE 2. OPTICAL/UV COUNTERPARTS TO *Chandra* X-RAY SOURCES

CX	GO ^a	$\Delta\alpha$ ($''$)	$\Delta\delta$ ($''$)	Δ (σ)	U_{336}	V_{555}	I_{814}
1	6116	0.24	-0.14	2.0	...	17.37(1)	16.19(1)
2	5461	-0.02	-0.19	1.2	23.65(6)	24.05(3)	22.29(3)
	8153	0.08	-0.07	0.7	22.04(1)
3	6116	0.12	-0.00	0.8	...	17.22(1)	15.90(1)
	5461	0.19	-0.05	1.3	18.00(1)	sat.	sat.
	5461	0.16	0.04	1.1	17.94(1)	sat.	sat.
	8153	0.20	0.02	1.4	15.94(1)
	8153	0.05	0.06	0.6	18.94(1) ^b
4	6116	0.12	-0.01	0.8	...	21.69(3)	19.79(2)
10	6116	-0.09	-0.21	1.2	...	16.78(1)	15.29(1)
12	6116	0.02	-0.00	0.1	...	24.2(2)	23.2(2)
	5461	0.08	0.03	0.5	24.01(8)	24.17(2)	23.45(4)
	8153	0.11	0.02	0.7	23.49(3)
13	6116	-0.08	0.03	0.4	...	18.11(1)	16.51(1)
18	5461	-0.09	-0.05	0.4	17.76(1)	sat.	sat.
	8153	-0.03	-0.04	0.2	15.64(1)
20	6116	0.24	-0.13	1.1	...	18.34(1)	17.05(1)
	5461	0.25	-0.15	1.1	19.62(1)	sat.	sat.
	8153	0.26	-0.08	1.1	17.04(1)
22	6116	0.11	-0.03	0.5	...	16.73(1)	15.50(2)
24	5461	0.08	-0.46	1.8	und.	23.49(1)	19.93(1)
	5461	0.14	-0.52	2.1	und.	24.4(1)	20.40(3)
	8153	0.23	-0.38	1.8	19.93(1)
	8153	0.20	-0.38	1.7	20.02(1)
25	6116	0.09	0.14	0.8	...	19.45(3)	17.75(1)
26	6116	-0.03	-0.10	0.5	...	19.18(1)	17.66(1)
	5461	sat.	sat.	sat.
	5461	0.02	-0.05	0.2	20.23(1)	sat.	sat.
	8153	0.06	-0.09	0.5	17.83(1)
	8153	0.06	-0.09	0.5	17.76(2)
27	6116	-0.16	-0.18	0.8	...	18.06(1)	16.65(1)
28	6116	0.29	0.11	1.3	...	19.16(1)	17.61(1)

NOTE. — Optical positions and magnitudes of the candidate counterparts. The optical positional is given by the *Chandra* value plus offset (in true seconds of arc) in each coordinate. Magnitude uncertainties are given in parentheses and refer to the last quoted digit. Stars that were saturated in a pass band are denoted with “sat.” and stars that are not detected in a band are denoted with “und.”

^aThe *HST* GO dataset number from which the position and magnitudes are determined. For CX3, CX24 and CX26 the first entry for dataset GO5461 and GO8153 refers to the field nearest to the cluster center.

^bThis measurement is likely in error due to the proximity of the star to the edge of the chip.

quence or giant branch are identified as candidate counterparts and are numbered in Fig. 4. Positional and color information for each candidate counterpart is tabulated in Table 2. Finding charts are shown in Figure 5.

3.4. Identification of counterparts in the WFI image

Several of *Chandra* X-ray sources coincide with stars on the WFI image. Two of these stars, identified by Mochejska et al. (2002) as variables V52 and V56 are coincident with X-ray sources CX8 and the possibly blended source CX5-9, respectively. The offset of the optical positions with respect to the *Chandra* positions in Table 1 is $0''.06 \pm 0''.20$, $0''.22 \pm 0''.21$ for CX8 and V52, $-0''.29 \pm 0''.22$, $-0''.23 \pm 0''.21$ for CX5 and V56 and

$0''.73 \pm 0''.20$, $0''.55 \pm 0''.21$ for CX9 and V56.

The X-ray source CX7 coincides with the UCAC1 star 22560073, a foreground star according to its proper motion (Cudworth & Rees 1990, star A330 with $V = 12.68$). The offset of the corrected X-ray position, as listed in Table 1, from the optical position from UCAC is $0''.38 \pm 0''.18$ in right ascension and $-0''.16 \pm 0''.20$ in declination. The error in this offset is dominated by the uncertainty in the X-ray position of CX7 in the *Chandra* frame; much smaller contributions to the error are due to the uncertainties in the X-ray to optical shift and in the optical position. Redetermining the X-ray to optical shift including CX7 with the other three optically identified X-ray sources, does not significantly change the value of the shift.

4. SOURCE CLASSIFICATION

In attempting to classify the X-ray sources detected in M4, we note that five of our optical counterparts to *Chandra* sources have a previously known classification. CX12 is a millisecond pulsar with a white dwarf companion (Thorsett et al. 1999); the optical counterpart corresponds to the white dwarf (Sigurdsson et al. 2003, see also Fig. 4). CX13/V49, CX15/V48 and CX18/V55 are contact binaries, and CX8/V52 is a BY Dra system, i.e. these four sources are all magnetically active binaries (Kaluzny et al. 1997; Mochejska et al. 2002). The optical counterparts to CX13 and CX15 as identified from the ground based data, have both been resolved into multiple objects with *HST*/WFPC2. Kaluzny et al. (1997) noted that the optical counterpart to CX13, was brighter than expected for a contact binary with its period, placed at the distance and reddening of M4. This discrepancy is removed as our counterpart to CX13 is about a magnitude fainter than the blend (we note that the optical counterpart to CX13 appears to be too bright to be on the binary main sequence as it is about a magnitude brighter than a star on the main sequence with the same color, Figure 4). For the optical counterpart of CX15 the opposite appears to be the case. It was seen as a cluster member by Kaluzny et al. (1997), but *HST*/WFPC2 observations indicate that V48 is a blend of 3 or 4 stars. Hence, the contact binary is too faint to be a member, and may be a background object.

The possible blend of CX5 and CX9 coincides with the variable giant V56 found by Mochejska et al. (2002). If the giant is a member of a RS CVn binary then its variability and X-ray emission can be explained by magnetic activity. However, without more information on the optical properties of V56 the classification remains ambiguous.

In classifying the remaining X-ray sources we first look at the X-ray emission itself. A neutron star accreting at a low rate from a companion star, i.e. a low-luminosity (quiescent) low-mass X-ray binary (qLMXB), is characterized by a soft X-ray spectrum (black body color temperature $\lesssim 0.3$ keV) and a luminosity $L_x \gtrsim 10^{32}$ erg s⁻¹ (Verbunt et al. 1994; Rutledge et al. 1999). None of the X-ray sources in our sample shows this characteristic, and we conclude that M4 does not contain a low-luminosity low-mass X-ray binary with an accreting neutron star.

We extract further information from the location of the optical star in the color-magnitude diagrams of Fig. 4:

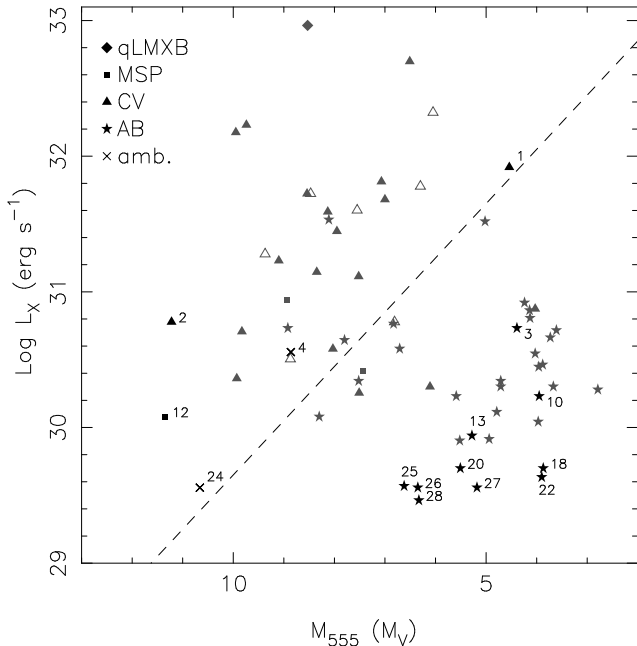


FIG. 6.— The X-ray luminosity L_x (0.5–2.5 keV) and the absolute V_{555} (approximately V -band) magnitude for X-ray sources with identified optical counterparts. Five types of X-ray sources are shown, quiescent LMXBs (*diamonds*), MSPs (*squares*), CVs (*triangles*), ABs (*stars*) and unclassified (*crosses*). The closed points are sources from 47 Tuc (Grindlay et al. 2001, Edmonds et al. 2003a) and the open points are from NGC 6752 (Pooley et al. 2002). The numbered points are the optical counterparts to the *Chandra* X-ray sources in M4, the number corresponds to the source number. The absolute magnitude of the optical counterparts is computed from the V_{555} magnitudes and the V -band distance modulus as in Harris (1996) for 47 Tuc and NGC 6752 and that of Richer et al. (1997) for M4. The dashed line of constant X-ray to optical flux ratio roughly separates cataclysmic variables from active binaries.

stars bluer than the main-sequence are possible cataclysmic variables, stars above the main-sequence possible magnetically active binaries. The ratio of X-ray to optical flux is also useful, as it roughly separates the cataclysmic variables from magnetically active binaries (Verbunt & Johnston 2000; Pooley et al. 2002a). We illustrate this in Fig. 6, where we plot data from 47 Tuc (Edmonds et al. 2003a,b) and NGC 6752 (Pooley et al. 2002a), and add our data from M4.

CX2 is a probable cataclysmic variable, because it is blue (Fig. 4) and has a relatively high X-ray to optical flux ratio (Fig. 6). High X-ray to optical flux ratios suggest that CX1 and CX4 also are cataclysmic variables, even though they are located on or close to the main sequence in the color-magnitude diagram (Fig. 4).

The X-ray luminosity of CX1 is too high for a magnetically active binary of two main sequence stars (i.e. a BY Dra system), and its optical magnitude excludes that it is a magnetically active binary with a sub-giant (i.e. a RS CVn system). This, and the relative hardness of the X-ray spectrum (Fig. 3) indicate that it is a cataclysmic variable. We note that the optical counterpart to CX1 is offset from the *Chandra* position by 2σ and might be a chance coincidence. This would indicate that the actual optical counterpart is even fainter, possibly lost in the glare of the bright star, leading to higher X-ray to optical flux ratios, as seen with most other CVs.

The less luminous counterpart to CX4 is probably a cataclysmic variable; its location near the main-sequence in $V_{555} - I_{814}$ has precedents in other globular clusters (Edmonds et al. 2003a,b).

The optical counterpart of CX24 varies by more than a magnitude in brightness (Fig. 4). It is located further above or to the right of the main-sequence than the binary sequence. Hence we believe that CX24 is either a foreground or background object and unrelated to M4. The same argument could be made for CX10. However, stars at similar positions in the color-magnitude diagram of other old clusters are X-ray sources and confirmed members (albeit unexplained, see e.g. Mathieu et al. 2003 for M67 and Orosz & van Kerkwijk 2003 for NGC 6397) or probable members (Albrow et al. 2001, Edmonds et al. 2003a for 47 Tuc). We therefore consider CX10 a probable cluster member.

Based on positional coincidence we identify CX7 with the UCAC1 star 22560073. This star has $V = 12.68$, $B - V = 0.88$ (Cudworth & Rees 1990), which is compatible with a K2V star at a distance of about 200 pc. Scaling the X-ray luminosity from Table 1 from the distance of M4 to a distance of 200 pc gives $L_x \approx 2.4 \times 10^{28}$ erg s $^{-1}$, well within the range observed for ordinary K2V stars (Verbunt 2001).

The relatively low X-ray to optical flux ratios of the remaining optical counterparts found with *HST*/WFPC2 suggests that they are active binaries. The counterparts of CX13 and CX18, already known to be contact binaries from ground based data, are among these. (The V_{555} image of the optical counterpart of CX18 is over-exposed; we use the estimate $V_{555} = (U_{336} + I_{814})/2$.) The others (CX3, CX20, CX22, CX25, CX26, CX27, CX28) are at or above the main-sequence, as expected for binaries, and we conclude that all of them are magnetically active binaries. The X-ray-to-optical flux ratio of any of the 2 candidate counterparts of CX21 is comparable to that of an active binary.

5. DISCUSSION

The X-ray luminosities of the *Chandra* sources in M4 are amongst the lowest ever observed in a globular cluster. More than half of the X-ray sources in this cluster have $L_x < 10^{30}$ erg s $^{-1}$, compared to 10% of the sources in 47 Tuc (Grindlay et al. 2001a) and 28% of the sources in NGC 6397 (Grindlay et al. 2001b).

It is therefore not surprising that only one of the X-ray sources detected with *Chandra* may have been detected before. The position of the marginal *ROSAT* HRI source R9 (Verbunt 2001) is $7''.5$ from that of CX1. Even though this is further than expected from the error given for the *ROSAT* HRI source, we think the identification is probable. The X-ray luminosity of the *ROSAT* HRI source is only 1.3×10^{31} erg s $^{-1}$, a factor six below the luminosity detected with *Chandra*. The upper limit from the *ROSAT* PSPC observation is 1.5×10^{31} erg s $^{-1}$. (These luminosities are re-computed for a distance of 1.73 kpc and for the spectrum of CX1, and thus differ from those given by Verbunt; mainly because he used a distance of 2.2 kpc.) This large variability indicates that CX1 is a cataclysmic variable rather than a radio pulsar. Note that even if the *ROSAT* source is not identical to CX1, it still provides an upper limit to the flux of CX1 during the *ROSAT* observations, and thus proves that CX1 is

TABLE 3. SCALING PARAMETERS OF M4, NGC 6397 AND 47 TUC

Cluster	$\log \rho_0$ ($L_\odot \text{ pc}^{-3}$)	r_c ($''$)	d (kpc)	M_V	Γ	M_c
M4	4.01	49.8	1.73	-6.9	1.0	1.0
NGC 6397	5.68	3.0	2.3	-6.6	2.1	0.024
47 Tuc	4.81	24.0	4.5	-9.4	24.9	12.4

NOTE. — Values for central density (ρ_0), core-radius (r_c), distance (d) and absolute visual magnitude (M_V) originate from Harris 1996 (version of February 2003). For M4, the values of ρ_0 and M_V are computed for the distance and reddening of Richer et al. (1997). The collision number is computed from $\Gamma \propto \rho_0^{1.5} r_c^2$ and the core mass from $M_c \propto \rho_0 r_c^3$. Values for Γ and M_c are normalized to the value of M4.

highly variable.

Several other X-ray sources coincide with optical variables discovered by Kaluzny et al. (1997) and Mochejska et al. (2002). The sources CX13, CX15 and CX18 are coincident with W UMa variables V49, V48 and V55, with orbital periods of 0.283, 0.298 and 0.311 days, respectively. The upper limit on the X-ray luminosity of the other W UMa binaries found by Kaluzny et al. (1997), V44, V47, V50, V51, V53 and V54, is about $3 \times 10^{29} \text{ erg s}^{-1}$. Both detections and upper limits of these W UMa variables are in agreement with the range of X-ray luminosities of W UMa binaries in the *ROSAT* All Sky Survey (Stępień, Schmitt & Voges 2001).

CX8 coincides with the variable V52, which is classified as a BY Dra system with a period of 0.777 days. The possible blend of X-ray sources CX5 and CX9 coincides with the variable V56. No period is known for this object, but its variability (a rise of 0.1 mag in 4 days) and its location on the giant branch (Mochejska et al. 2002) are suggestive of an RS CVn variable. If it is, it is the first RS CVn binary detected in X-rays in a globular cluster – a marked contrast with old open clusters, where RS CVns dominate the X-ray sources (Belloni et al. 1998). The exposure of the eclipsing binary V54 is not as good as for the other sources, hence the upper limit on the X-ray luminosity of this source is somewhat higher. Detections and upper limits of these binaries are well within the range observed for magnetically active binaries, e.g. in the *ROSAT* All Sky Survey (Dempsey et al. 1993).

In trying to determine the X-ray luminosity function of M4, we can use the number of detected sources as a function of luminosity. However, the number of excess counts, not allocated to individually detected sources, also contains information about the luminosity function. If we assume a luminosity function $dN \propto L_x^{-\gamma} d \log L_x$ and a reference luminosity L_r , then the ratio of the contributions to the total luminosity by sources in the ranges $(0.1-1)L_r$ and $(1-10)L_r$ is given by

$$R_L(L_r) \equiv \frac{\int_{0.1L_r}^{L_r} L_x dN}{\int_{L_r}^{10L_r} L_x dN} = 10^{\gamma-1} \quad (1)$$

and the ratio of the number of sources in the same ranges is

$$R_N(L_r) = 10^\gamma = 10R_L(L_r). \quad (2)$$

In particular, we note that for $\gamma < 0.7$ and a luminosity function continuing to arbitrarily low luminosities the total luminosity of all sources with $L_x < L_r$ is less than the

luminosity for the sources with $(1-10)L_r$. In the following we assume that the ratio of counts is proportional to the ratio of luminosities, and we use as a reference luminosity $L_r \equiv 6 \times 10^{29} \text{ erg s}^{-1}$.

Following the method described in Johnston & Verbunt (1996) and Pooley et al. (2002b) we derive from the list of detected X-ray sources (Table 1) that $\gamma = 0.71$ for X-ray luminosities above $L_x(0.5 - 2.5) = 4.4 \times 10^{29} \text{ erg s}^{-1}$. The K-S probability of this value is 93%. For K-S probabilities above 10% the slope of the luminosity function has $0.47 < \gamma < 1.07$.

In addition to the detected sources, we have an excess in the core of M4 of about 150 counts, uncorrected for absorption, which corresponds to roughly 300 counts corrected for absorption in the 0.5–6.0 keV band (which is the addition of counts in X_{soft} and in X_{hard}). In this band, the five faintest sources in the core, CX20, CX21, CX22, CX26 and CX27 have between 14 and 10 counts. A minimum number of sources required to explain the excess counts is found by assuming that each source has 10–14 counts, which gives 22–30 sources.

The total number of ~ 350 counts from sources in the core of M4 with $L_x < L_r$ (five detected sources and the excess) is similar to that of the 6 sources in the range $(1-10)L_r$. From our remark following Eqs. 1 and 2, we see that this implies that $\gamma \geq 0.7$; for lower values of γ the sources with $L_x < L_r$ do not contribute enough counts to explain the observed number. On the other hand, for $\gamma = 1$ the luminosity function must have a cutoff near $0.1L_r$, because otherwise the sources with $L_x < L_r$ would produce more counts than is observed. With 6 sources in the range $(1-10)L_r$, and for $\gamma = 0.7 - 1.0$ we have 30–60 core sources in the range $(0.1-1)L_r$.

In the core of 47 Tuc there are 14 sources in the range $(10-100)L_r$, which for $\gamma = 0.7 - 0.8$ leads to predicted numbers of 70–90 (of which 27 are already detected individually) in the range $(1-10)L_r$, and 350–560 in the range $(0.1-1)L_r$. These numbers are compatible with the total number of counts in the core of 47 Tuc from the observed sources plus the excess of about 500 counts, estimated by Grindlay et al. (2001a).

In Table 3 we compare the collision numbers and the masses of the cores of M4 and 47 Tuc. We expect that the numbers of cataclysmic variables scales with the collision number, and the number of magnetically active binaries with the mass. In the range $(1-10)L_r$ the ratio of numbers of sources in the cores of M4 and 47 Tuc suggest that the ratio is set by mass rather than collision number. This in turn suggests that magnetically active binaries dominate the numbers at these luminosities, in agreement with our suggested identifications in M4.

Comparison with NGC 6397 is also interesting, as its collision number is somewhat higher, $\Gamma = 2.1$ (normalized to the value of M4) while its total mass (as measured from its absolute magnitude) is somewhat lower than that of M4. Within its half-mass radius, NGC 6397 contains 9 cataclysmic variables, 4 magnetically active binaries and 10 as yet unclassified sources (generally of low X-ray luminosity). Within the half mass radius of M4 we find 2 or 3 cataclysmic variables, 12 magnetically active binaries and 15 unclassified sources, of which an estimated 6–12 are background sources. The ratio for the numbers in NGC 6397 and M4 of magnetically active binaries is as expected for a scaling with mass. As already

noted by Pooley et al. (2003), NGC 6397 contains rather more cataclysmic variables than expected on the basis of its collision number. This is reflected in the flat slope of its X-ray luminosity function. If the high number of bright systems in NGC 6397 is explained by a higher mass of this cluster in the past (as suggested by Pooley et al. 2003), one would expect an accordingly higher number of magnetically active binaries, in contrast to what is observed (assuming that magnetically active binaries have a similar evaporation rate as cataclysmic variables, much lower than the evaporation rate of single stars). In this respect, it is worth noting that the time scale on which a binary can be destroyed by a close encounter is short in NGC 6397 compared to most other clusters, including M4 and 47 Tuc (Verbunt 2003, in particular Figure 3b). Since magnetically active binaries tend to have longer orbital periods than cataclysmic variables, they would be easier destroyed by close encounters. This might ex-

plain the absence of large numbers of such binaries in NGC 6397.

C.B. acknowledges support by the Netherlands organization for Scientific Research (NWO). D.P. and W.H.G.L. thank NASA for its support. L.H. and S.F.A. also gratefully acknowledge their support from NASA grant NAG5-7932. V.M.K. is supported by NSERC, NATEQ, CIAR and NASA. This research is based on observations made with the ESO Telescopes at the La Silla Observatory and observations made with the NASA/ESA Hubble Space Telescope, obtained from the data archive at the Space Telescope Institute. STScI is operated by the association of Universities for Research in Astronomy, Inc. under the NASA contract NAS 5-26555. Support for proposal #9959 was provided by NASA through grants from STScI.

REFERENCES

- Albrow, M. D., Gilliland, R. L., Brown, T. M., Edmonds, P. D., Guhathakurta, P., & Sarajedini, A. 2001, *ApJ*, 559, 1060
- Aldcroft, T. L., Karovska, M., Cresitello-Dittmar, M. L., Cameron, R. A., & Markevitch, M. L. 2000, in *Proc. SPIE Vol. 4012*, p. 650-657, X-Ray Optics, Instruments, and Missions III, Joachim E. Truemper; Bernd Aschenbach; Eds., ed. J. E. Truemper & B. Aschenbach, 650-657
- Anderson, J. & King, I. R. 2003, *PASP*, 115, 113
- Arnaud, K. A. 1996, in *ASP Conf. Ser. 101: Astronomical Data Analysis Software and Systems V*, ed. G. H. Jacoby & J. Barnes, 17
- Assafin, M., Zacharias, N., Rafferty, T. J., Zacharias, M. I., da Silva Neto, D. N., Andrei, A. H., & Vieira Martins, R. 2003, *AJ*, 125, 2728
- Bassa, C. G., Verbunt, F., van Kerkwijk, M. H., & Homer, L. 2003, *A&A*, 409, L31
- Bedin, L. R., Anderson, J., King, I. R., & Piotto, G. 2001, *ApJ*, 560, L75
- Bedin, L. R., Piotto, G., King, I. R., & Anderson, J. 2003, *AJ*, 126, 247
- Belloni, T., Verbunt, F., & Mathieu, R. 1998, *A&A*, 339, 431 (erratum: 351, 398)
- Biretta, J. A., e. a. 2000, *WFPC2 Instrument Handbook Version 5.0* (Baltimore, STScI)
- Cudworth, K. M. & Rees, R. 1990, *AJ*, 99, 1491
- Dempsey, R., Linsky, J., Fleming, T., & Schmitt, J. 1993, *ApJS*, 86, 599
- Dolphin, A. E. 2000a, *PASP*, 112, 1397
- , 2000b, *PASP*, 112, 1383
- Edmonds, P. D., Gilliland, R. L., Heinke, C. O., & Grindlay, J. E. 2003a, *ApJ*, 596, 1177
- , 2003b, *ApJ*, 596, 1197
- Fabian, A. C., Pringle, J. E., & Rees, M. J. 1975, *MNRAS*, 172, 15P
- Giacconi, R., Rosati, P., Tozzi, P., Nonino, M., Hasinger, G., Norman, C., Bergeron, J., Borgani, S., Gilli, R., Gilmozzi, R., & Zheng, W. 2001, *ApJ*, 551, 624
- Grindlay, J., Heinke, C., Edmonds, P., , & Murray, S. 2001a, *Science*, 292, 2290
- Grindlay, J., Heinke, C., Edmonds, P., , Murray, S., & Cool, A. 2001b, *ApJ*, 563, L53
- Harris, W. 1996, *AJ*, 112, 1487
- Hertz, P. & Grindlay, J. 1983, *ApJ*, 275, 105
- Hills, J. G. 1976, *MNRAS*, 175, 1P
- Johnston, H. & Verbunt, F. 1996, *A&A*, 312, 80
- Kaluzny, J., Thompson, I. B., & Krzeminski, W. 1997, *AJ*, 113, 2219
- Lyne, A., Biggs, J., Brinklow, A., Ashworth, & McKenna, J. 1988, *Nature*, 332, 45
- Mathieu, R. D., van den Berg, M., Torres, G., Latham, D., Verbunt, F., & Stassun, K. 2003, *AJ*, 125, 246
- Mochejska, B. J., Kaluzny, J., Thompson, I., & Pych, W. 2002, *AJ*, 124, 1486
- Orosz, J. A. & van Kerkwijk, M. H. 2003, *A&A*, 397, 237
- Pooley, D., Lewin, W., Homer, L., Verbunt, F., Anderson, S., Gaensler, B., Margon, B., Miller, J., Fox, D., Kaspi, V., & van der Klis, M. 2002a, *ApJ*, 569, 405
- Pooley, D., Lewin, W., Verbunt, F., Homer, L., Margon, B., Gaensler, B., Kaspi, V., Miller, J., Fox, D., & van der Klis, M. 2002b, *ApJ*, 573, 184
- Pooley, D., Lewin, W. H. G., Anderson, S. F., Baumgardt, H., Filippenko, A. V., Gaensler, B. M., Homer, L., Hut, P., Kaspi, V. M., Makino, J., Margon, B., McMillan, S., Portegies Zwart, S., van der Klis, M., & Verbunt, F. 2003, *ApJ*, 591, L131
- Predehl, P. & Schmitt, J. 1995, *A&A*, 293, 889
- Richer, H., Fahlman, G., Ibata, R., & et. al. 1995, *ApJ*, 451, L17
- Richer, H. B., Fahlman, G. G., Ibata, R. A., Pryor, C., Bell, R. A., Bolte, M., Bond, H. E., Harris, W. E., Hesser, J. E., Holland, S., Ivanans, N., Mandushev, G., Stetson, P. B., & Wood, M. A. 1997, *ApJ*, 484, 741
- Richer, H. B., Ibata, R., Fahlman, G. G., & Huber, M. 2003, *ApJ*, 597, L45
- Rutledge, R., Bildsten, L., Brown, E., Pavlov, G., & Zavlin, V. 2002, *ApJ*, 578, 405
- Rutledge, R. E., Bildsten, L., Brown, E. F., Pavlov, G. G., & Zavlin, V. E. 1999, *ApJ*, 514, 945
- Sigurdsson, S., Richer, H. B., Hansen, B. M., Stairs, I. H., & Thorsett, S. E. 2003, *Science*, 301, 193
- Stepień, K., Schmitt, J. H. M. M., & Voges, W. 2001, *A&A*, 370, 157
- Thorsett, S., Arzoumanian, Z., Camilo, F., & Lyne, A. 1999, *ApJ*, 523, 763
- Verbunt, F. 2001, *A&A*, 368, 137
- Verbunt, F. 2003, in *New horizons in globular cluster astronomy*, ed. S. D. G. Piotto, G. Meylan & M. Riello (ASP Conf. Ser. Vol. 296), 245-254
- Verbunt, F., Belloni, T., Johnston, H., van der Klis, M., & Lewin, W. 1994, *A&A*, 285, 903
- Verbunt, F. & Hut, P. 1987, in *The Origin and Evolution of Neutron Stars*, IAU Symposium No. 125, ed. D. Helfand & J.-H. Huang (Dordrecht: Reidel), 187-197
- Verbunt, F. & Johnston, H. 2000, *A&A*, 358, 910
- Zacharias, N., Urban, S. E., Zacharias, M. I., Hall, D. M., Wycoff, G. L., Rafferty, T. J., Germain, M. E., Holdenried, E. R., Pohlman, J. W., Gauss, F. S., Monet, D. G., & Winter, L. 2000, *AJ*, 120, 2131